ATMOSPHERIC SCIENCE

Persistent and enhanced carbon sequestration capacity of alpine grasslands on Earth's Third Pole

Yuyang Wang[1,2,3], Jingfeng Xiao[4], Yaoming Ma[1,3,5,6,7]*, Jinzhi Ding[1], Xuelong Chen[1]*, Zhiyong Ding[8], Yiqi Luo[9]

The carbon sequestration capacity of alpine grasslands, composed of alpine meadows and steppes, in the Tibetan Plateau has an essential role in regulating the regional carbon cycle. However, inadequate understanding of its spatiotemporal dynamics and regulatory mechanisms restricts our ability to determine potential climate change impacts. We assessed the spatial and temporal patterns and mechanisms of the net ecosystem exchange (NEE) of carbon dioxide in the Tibetan Plateau. The carbon sequestration of the alpine grasslands ranged from 26.39 to 79.19 Tg C year^{-1} and had an increasing rate of 1.14 Tg C year^{-1} between 1982 and 2018. While alpine meadows were relatively strong carbon sinks, the semiarid and arid alpine steppes were nearly carbon neutral. Alpine meadow areas experienced strong increases in carbon sequestration mainly because of increasing temperatures, while alpine steppe areas had weak increases mainly due to increasing precipitation. Carbon sequestration capacity of alpine grasslands on the plateau has undergone persistent enhancement under a warmer and wetter climate.

INTRODUCTION

Terrestrial ecosystems, one of the crucial carbon sinks of Earth, sequester about one-third of the carbon dioxide (CO_2) released by human activities, having considerably mitigated global warming (1). The net ecosystem exchange (NEE) of CO_2, i.e., the difference between the CO_2 fixed by plants via photosynthesis and the CO_2 released via ecosystem respiration, reflects to what extent an ecosystem functions as a carbon source or sink (2). The quantification of NEE at the regional and global scales is of vital importance to accurately estimate the terrestrial carbon budget and to gain better understanding of the carbon cycle and carbon-climate feedbacks (3). However, the lack of in situ observations and inadequate mechanistic understandings lead to large uncertainties about NEE at the regional scale. Therefore, it is urgent to accurately estimate regional-scale NEE and understand the mechanisms underlying its spatial-temporal variations by using robust methods to upscale ground-based observations.

Ecosystem-scale NEE can be continuously measured in situ with eddy covariance technique and has been used to estimate the regional NEE, mainly using model-based and data-driven approaches (4). Model-based approaches are usually based on ecosystem models that use observations and/or remote sensing data to optimize the model parameters (5). The resulting models are then used to upscale NEE to the regional level. However, most ecosystem models rely on local parameters, which may limit the accuracy of simulations at larger scales and increase the uncertainty of the resulting regional NEE estimates. Alternatively, the data-driven approach is based on statistical models and extends in situ NEE measurements to the regional scale by constructing statistical relationships between observed values and the explanatory variables (6). Although data-driven approaches differ from the model-based approaches in that they do not explicitly consider biogeochemical processes, they do not subjectively impose conditions on the validity range of model parameters during training, and their performance in estimating regional NEE value is reliable. Therefore, on the basis of flux measurements and relevant satellite remote sensing observations, data-driven methods have been widely used to upscale observed carbon fluxes to regional and global scales (7–10).

The Tibetan Plateau (TP) is known as the Third Pole of Earth due to its unique terrain (11). Alpine grassland, an alpine ecosystem in which the characteristic plants are grasses, is the main vegetation type on the TP, with a total area of approximately 1.46 million km^2 (12). The grasslands on the TP are mainly divided into two categories: alpine steppe and alpine meadow. Alpine steppes, with drought-tolerant species, are distributed in the relatively arid west and north of the plateau, while alpine meadows that are dominated by mesic and meso-xeric species are distributed in the relatively humid central and east regions (13). Alpine grassland ecosystems on the TP are extremely vulnerable and sensitive to climate change due to the high altitude and cold, semiarid climate with strong solar radiation and winds, poor soil quality, and short growing season (14). Previous studies have shown that the climate warming rate on the TP is approximately twice the global rate and that precipitation has also shown a significant increasing trend. As a result, the plateau climate is becoming warmer and wetter (15, 16). Under these conditions, grassland productivity has increased. In addition, the intensity of human activities in recent decades, such

[1]Land–Atmosphere Interaction and its Climatic Effects Group, State Key Laboratory of Tibetan Plateau Earth System Science, Environment and Resources (TPESER) „ Institute of Tibetan Plateau Research, Chinese Academy of Sciences, Beijing 100101, China. [2]Sino-French Institute for Earth System Science, College of Urban and Environmental Sciences, Peking University, Beijing 100871, China. [3]College of Earth and Planetary Sciences, University of Chinese Academy of Sciences, Beijing 100049, China. [4]Earth Systems Research Center, Institute for the Study of Earth, Oceans, and Space, University of New Hampshire, Durham, NH 03824, USA. [5]National Observation and Research Station for Qomolongma Special Atmospheric Processes and Environmental Changes, Dingri 858200, China. [6]Kathmandu Center of Research and Education, Chinese Academy of Sciences, Beijing 100101, China. [7]College of Atmospheric Science, Lanzhou University, Lanzhou 730000, China. [8]State Key Laboratory of Geohazard Prevention and Geoenvironment Protection, Chengdu University of Technology, Chengdu 610059, China. [9]School of Integrative Plant Science, Cornell University, Ithaca, NY 14853, USA.
*Corresponding author. Email: ymma@itpcas.ac.cn (Y.M.); x.chen@itpcas.ac.cn (X. C.)

as fence construction and grazing, has increased; nitrogen deposition has also shown an obvious increase; and permafrost thaw has become intense, which has aggravated the degradation of alpine grasslands ([17–19]). These changes have exacerbated the ecological vulnerability of the region, leading to increased uncertainty about the carbon cycle ([20]). Warming can not only increase gross primary productivity (GPP) and lengthen the growing season but also enhance ecosystem respiration. Thus, there are many uncertainties around these two processes that make it challenging to quantify NEE changes in the TP.

Given the crucial significance of the carbon cycle on the TP in the context of the global climate change, many scholars have already used models to assess NEE in the TP ([21], [22]). In general, these models have large discrepancies in both the magnitude and spatial distribution of their estimates. This is mainly due to the fact that large amounts of data, such as flux observations, are required to drive carbon cycle models and to calibrate model parameters, but the scarcity and uneven distribution of ground-based observations on the TP often lead to inaccurate parameter calibration ([23]). In recent decades, more flux observation stations have been set up in the alpine region of the TP, providing strong data support for upscaling NEE ([24–26]). Integrating these observations and data-driven approaches can help us explore the spatial and temporal patterns of the NEE and to better understand the carbon dynamics in the alpine grasslands in the TP in the context of climate change.

The alpine steppes of the TP are typically water limited, while alpine meadows tend to be temperature limited ([27]). Thus, a warmer and wetter climate will alleviate restrictions to plant growth. However, it remains unclear how carbon sequestration capacity has changed during the past few decades. In this study, we applied the extremely randomized trees regression (ETR) algorithm to estimate the annual NEE on the TP at a $0.05° \times 0.05°$ spatial resolution during the period 1982–2018. The gridded NEE product was generated from in situ eddy covariance measurements, satellite remote sensing data, and meteorological data. Our main objectives were to explore the spatial and temporal patterns of NEE in the TP and to understand mechanisms of interannual NEE variations in the past 37 years.

RESULTS

Spatial and temporal patterns of the alpine grassland NEE on the TP

Temporally, the higher- and lower-resolution, gridded NEE datasets that we generated for a 19-year period (2000–2018) and a 37-year period (1982–2018), respectively, using eddy covariance measurements, satellite remote sensing data, and meteorological data, along with the ETR algorithm, were highly consistent for the TP alpine grasslands (Fig. 1E and fig. S1A). The correlation coefficient of the regional mean NEE between the two datasets over their overlapping period 2000–2018 was 0.96, and the root mean square error (RMSE) was 2.03 g C m^{-2} year^{-1}. The seasonal distributions of the two NEE datasets were also highly consistent, indicating a carbon sink in the growing season from May to September and a weak carbon source in the other months (Fig. 1F and fig. S1B). The lower-resolution NEE dataset over the period 2000–2018 revealed that the annual NEE of the alpine grassland region on the TP fluctuated between −57.08 and −32.47 g C m^{-2} year^{-1}, with an average

of −43.50 ± 5.34 g C m^{-2} year^{-1}, and showed a nonsignificant trend of −0.38 g C m^{-2} year^{-1} ($P > 0.05$). In addition, the regionally averaged annual NEE based on the higher-resolution NEE dataset ranged from −49.66 to −30.68 g C m^{-2} year^{-1}, with an average of −42.19 ± 4.80 g C m^{-2} year^{-1}, and also showed a nonsignificant trend of 0.20 g C m^{-2} year^{-1} ($P > 0.05$).

At the regional scale, the spatial distribution patterns of the higher- and lower-resolution NEE datasets for their overlapping period 2000–2018 were also largely consistent (fig. S2, A and C). The alpine meadows in the relatively humid eastern and northeastern parts of the TP were strong carbon sinks (−150 to −100 g C m^{-2} year^{-1}); the carbon sink strength gradually weakened along the longitudinal gradient, and arid and semiarid alpine steppes in the western and northern regions became weak carbon sinks or weak carbon sources (0 to ±20 g C m^{-2} year^{-1}). Patterns of NEE trend in the two datasets during their overlapping period (i.e., 2000–2018) were basically consistent and exhibited high spatial heterogeneity (fig. S2, B and D). In the alpine meadow region, the carbon sink intensity mostly showed a positive trend, while in some parts of the alpine steppe region, such as the Qiangtang Plateau, the absolute values of NEE showed a decreasing trend. However, the annual NEE trend was not significant ($P > 0.05$) for most grid cells across the study region. Regions with significant decreasing NEE were mainly distributed in the eastern and southwestern parts of the plateau, while regions with significant increasing NEE trends were primarily distributed in the central and northern parts of the plateau. Given the highly consistent temporal and spatial variations in the NEE of the alpine grassland on the TP between the higher- and lower-resolution datasets over their overlapping period (i.e., 2000–2018), we used only the NEE dataset based on the lower resolution, which had a much longer time series (1982–2018), to examine the spatial and temporal patterns of NEE on the TP over the 37-year period in the following analyses.

Over the 37-year period from 1982 to 2018, annual NEE averaged −35.59 ± 9.90 g C m^{-2} year^{-1} (−52.11 ± 14.50 Tg C year^{-1}), with a range from −18.02 to −54.08 g C m^{-2} year^{-1} (−26.39 to −79.19 Tg C year^{-1}) and a significant decreasing trend of −0.78 g C m^{-2} year^{-1} (−1.14 Tg C year^{-1}) (Fig. 1E). Since 1982–2018 was such a long period (i.e., 37 years), we also analyzed the spatial and temporal patterns of NEE over two subperiods: 1982–1999 and 2000–2018. Between 1982 and 1999, mean annual NEE was −27.25 ± 5.81 g C m^{-2} year^{-1} (−39.90 ± 8.51 Tg C year^{-1}) and had a significant trend of −0.62 g C m^{-2} year^{-1} (−0.91 Tg C year^{-1}). The net carbon uptake and its increase rate were both slightly lower during 1982–1999 than during the 37-year period. Overall, NEE patterns during 1982–1999 and 1982–2018 remained largely consistent with those of the 2000–2018 period (fig. S3A and Fig. 1C). In addition, the proportion of pixels showing carbon sources (>20%) was slightly larger during 1982–1999 than during 1982–2018 and 2000–2018. NEE showed a decreasing trend from 1982 to 1999, but areas with significant changes were small and scattered. By contrast, most of the study region was dominated by a decreasing trend (>60%) during 1982–2018. Again, such trends showed notable spatial heterogeneity, with the eastern alpine meadow region reaching −3 to −2 g C m^{-2} year^{-1} and the western alpine grassland region exhibiting significant decreasing trends of about −2 to 0 g C m^{-2} year^{-1} (Fig. 1D).

The interannual variability in seasonal NEE during the 37-year period between 1982 and 2018 is shown in Fig. 2. Alpine grasslands
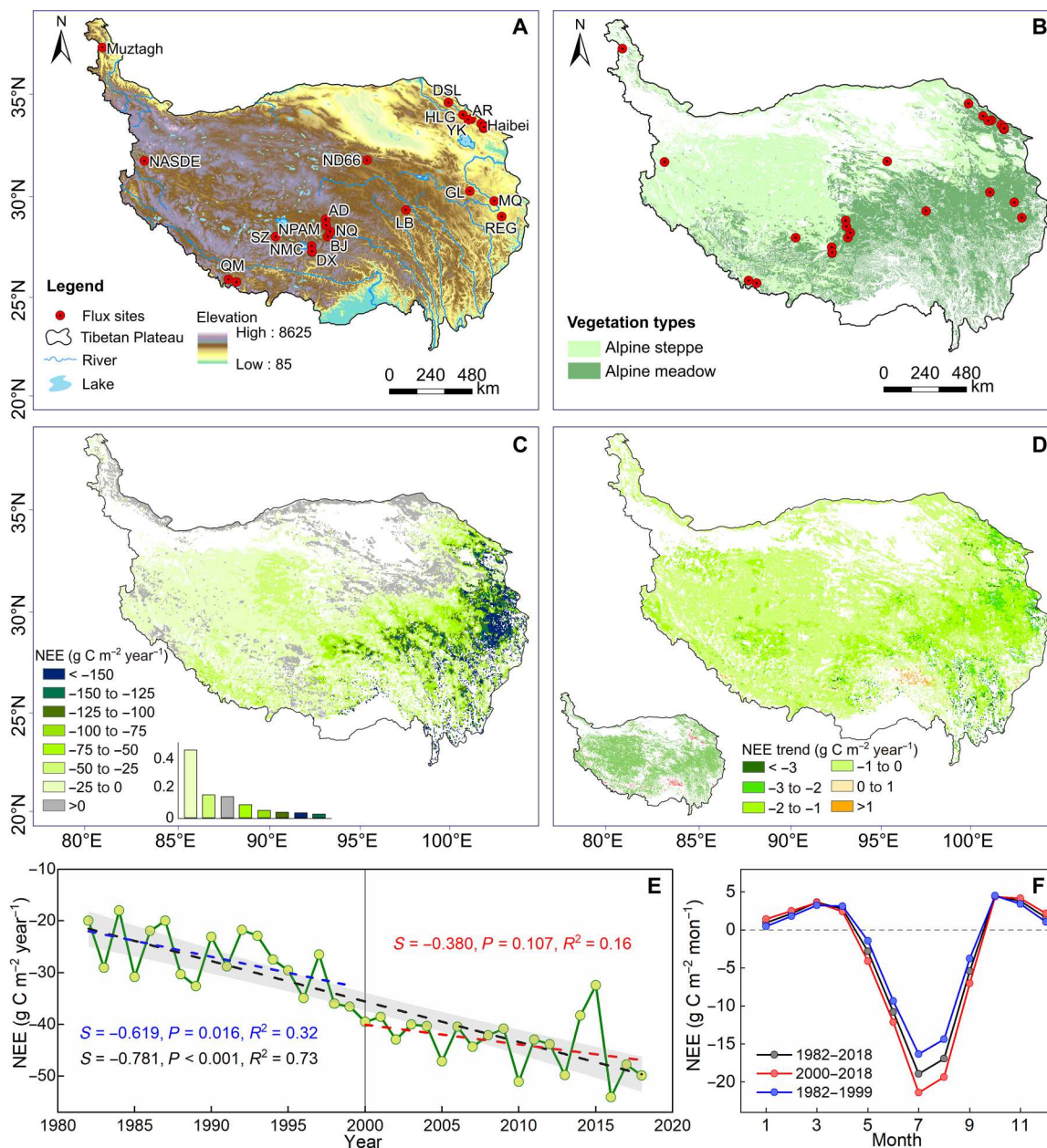
Fig. 1. Spatial predictions and temporal trends of the NEE in the alpine grasslands. (**A**) Flux site distribution for the NEE upscaling in the alpine grasslands on the TP and a topographic map. (**B**) Alpine grassland distribution map. Spatial distribution of the (**C**) mean annual NEE and (**D**) NEE trend during 1982–2018 at a 0.05° resolution. Inset in (D) indicates pixels with significant increasing (red) and decreasing (green) trend at $P < 0.05$. (**E**) Temporal changes in the regional annual average NEE during 1982–2018, while the shading indicates the 95% confidence interval, and (**F**) monthly averaged NEE during 1982–2018 at a 0.05° resolution. The black, blue, and red lines denote 1982–2018, 1982–1999, and 2000–2018, respectively.

on the TP exhibited strong carbon sinks in summer but almost weak carbon sources in the other seasons. The winter NEE of alpine grasslands in the TP increased significantly ($P < 0.01$) at a rate of 0.14 g C m^{-2} year^{-1} during this period (Fig. 2D), suggesting that the amount of CO_2 released from alpine grasslands outside the growing season was enhanced; NEE in spring, summer, and autumn showed a significant ($P < 0.01$) decreasing trend at −0.18, −0.61, and −0.13 g C m^{-2} year^{-1}, respectively, indicating that the carbon sink capacity of alpine grassland was strengthened in these seasons.

Drivers of spatiotemporal variability of the NEE of the alpine grasslands on the TP
The large heterogeneity of NEE is the result of a combination of changes in several climatic and biotic factors. We adopted separation method to analyze the contribution of each explanatory variable to the spatial variation in NEE to explore the leading factors
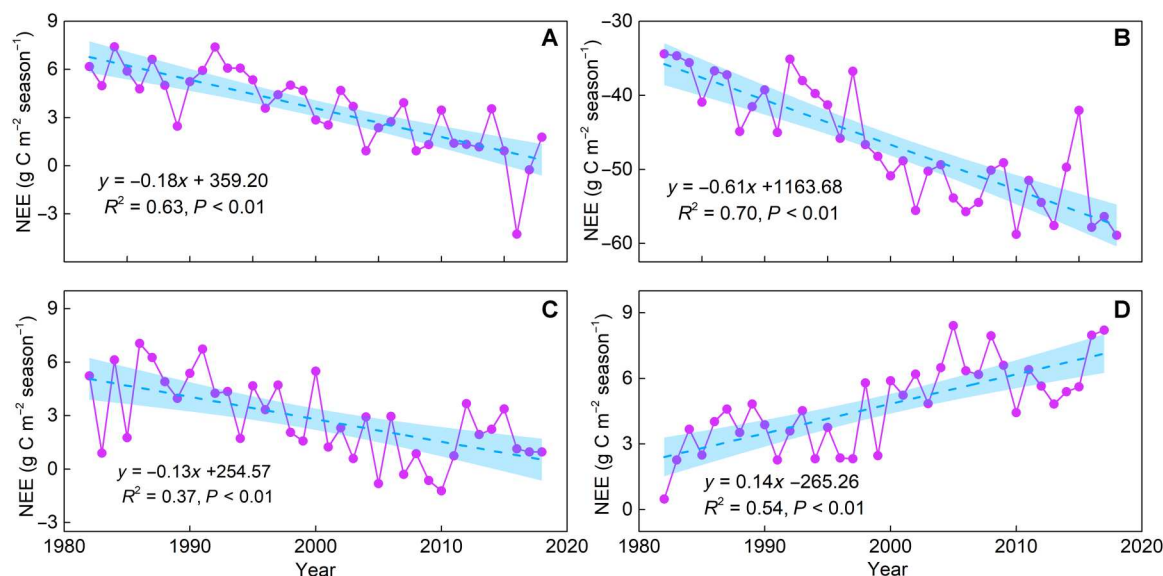
Fig. 2. Temporal variations of seasonal NEE in the alpine grasslands. (**A**) Spring, (**B**) summer, (**C**) autumn, and (**D**) winter. The dashed lines indicate the linear fit for the seasonal NEE, while the blue shading represents the 95% confidence band of the fits.

influencing interannual variation. The contribution of each explanatory variable to the long-term trend of the NEE during 1982–2018 is shown in Fig. 3 (A1 to E1). Overall, annual precipitation and mean temperature contributed notably to the trend of the alpine grassland NEE in terms of magnitude, while the contribution of other variables was almost negligible. Specifically, the contribution of precipitation was largest in the alpine steppe region of the western and northwestern areas of the plateau (Fig. 3A1), while the contribution of temperature was largest in the alpine meadow region on the eastern and southern areas of the plateau (Fig. 3B1). To better explain the relationship between them, scatterplots of variation trends on a pixel basis and their contributions to the NEE trend were examined on the basis of plant community types (steppe and meadow) (fig. S4, A1 to E1). In the alpine steppe region, precipitation made a remarkable contribution to the NEE trend, while the contributions of the other variables were limited. Regarding precipitation, in the alpine steppe regions (red line), more than 97% of the grid cells were plotted in the second and fourth quadrants, suggesting that the increase in precipitation led to the decrease in the NEE (i.e., the increase in net carbon uptake), while the increase in NEE (i.e., the decrease in net carbon uptake) was associated with a decrease in precipitation (fig. S4A1). In the alpine meadow region, mean temperature made a marked contribution to the NEE trend, and more than 95% of the grid cells were plotted in the second and fourth quadrants (fig. S4B1), indicating that the increase in the mean annual temperature led to the decrease in the NEE. Similar effects were observed for precipitation and radiation, but they made smaller contributions.

We used the same method to examine the dominant climatic factor controlling interannual variation of NEE during 1982–1999 and 2000–2018 (Fig. 3, A2-E2 and A3-E3). The results revealed that these two time periods remained largely consistent with the general trend. That is, mean temperature and precipitation were the dominant drivers of NEE interannual variation in alpine meadow and alpine steppe regions, respectively. However, compared with

1982–1999 and 1982–2018, the results in the steppe region during 2000–2018 were slightly different, as precipitation was positively correlated with NEE over a larger area (Fig. 3A3). For precipitation, the proportion of pixels plotted in the second (47.09%) and fourth (38.72%) quadrants exceeded 85% (fig. S4A3). However, the decrease in precipitation during 2000–2018 shifted some regions of the alpine steppe toward carbon sources.

To quantify the proportion of the areas dominated by diverse drivers, we calculated the absolute values of the contributions of the explanatory variables. During 1982–2018, precipitation was the dominant factor for 84% of the entire alpine steppe region, while temperature was the dominant factor for 55% of the entire alpine meadow region. Precipitation and temperature were the dominant factors for 54 and 30% of the entire alpine grassland region on the TP, respectively, while the other variables accounted for small proportions (Fig. 4, A and B). The basic patterns of precipitation and temperature dominated the interannual variations in the NEE in the alpine steppe and alpine meadow regions, respectively, and they did not change between 1982–1999 and 2000–2018. From 1982–1999 to 2000–2018, the proportion of the alpine steppe region for which precipitation was the dominant factor decreased from 53 to 48%, while the proportion of the alpine meadow region for which temperature was the dominant factor increased from 38 to 43% (Fig. 4, C to F). In general, the interannual variability of the NEE tended to be predominantly controlled by precipitation in the alpine steppe region while by temperature in the alpine meadow region.

On the basis of the attribution results of spatial trends, we further analyzed the relationship between interannual variation of NEE and dominant factors in the entire alpine grassland region and in alpine meadow and alpine steppe regions separately during 1982–2018. For the entire alpine grassland region, annual precipitation and annual temperature explained 80 and 62% of the NEE variations, respectively; precipitation accounted for a greater proportion because of the relatively larger water-limited area (Figs. 5, A and
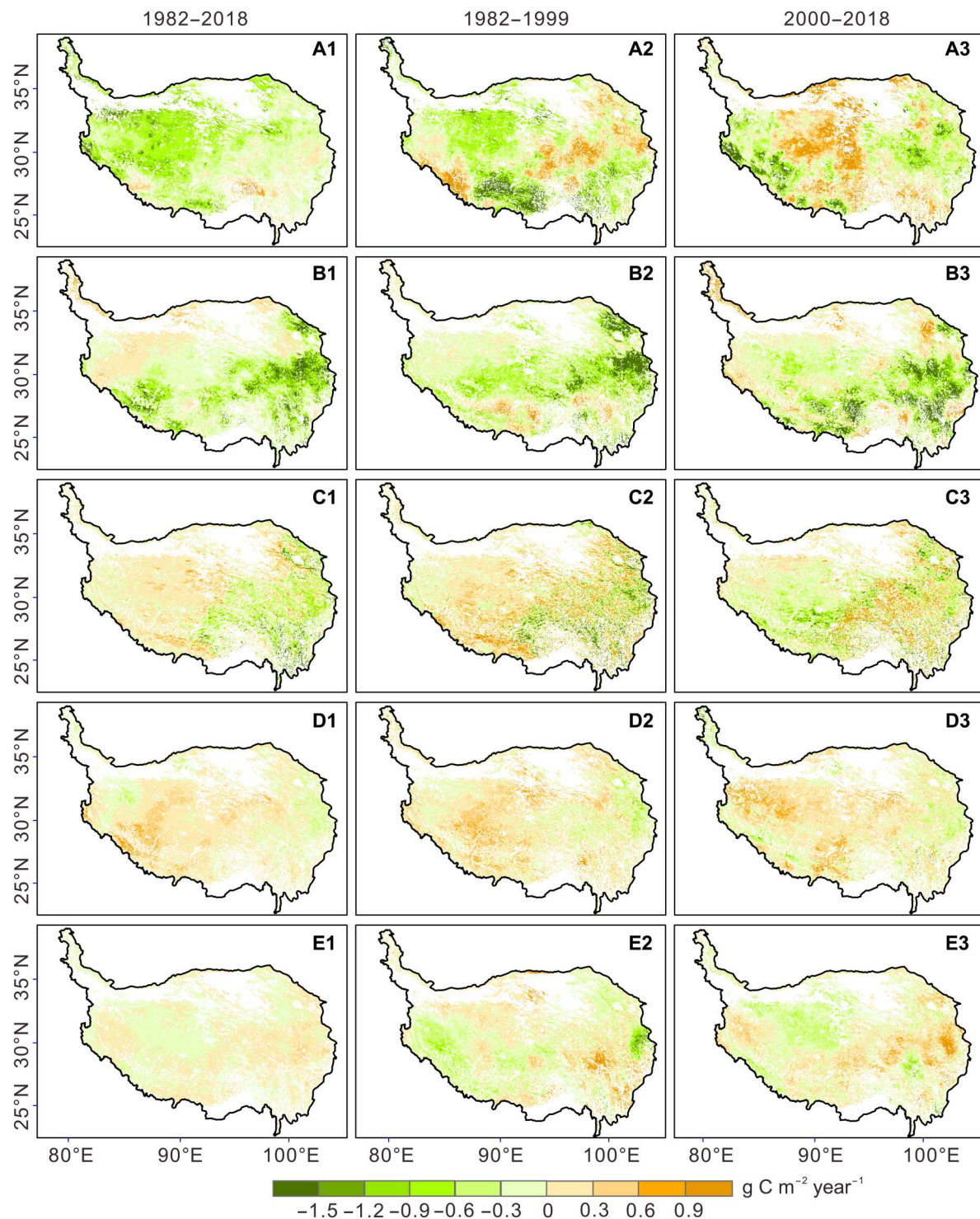
Fig. 3. Spatial distribution of the contribution of each explanatory variable to the NEE trends over the alpine grasslands during different periods. (**A1** to **A3**) Precipitation. (**B1** to **B3**) Mean air temperature. (**C1** to **C3**) Normalized difference vegetation index. (**D1** to **D3**) Maximum air temperature. (**E1** to **E3**) Downward shortwave radiation. The first to third columns refer to the periods of 1982–2018, 1982–1999, and 2000–2018, respectively.
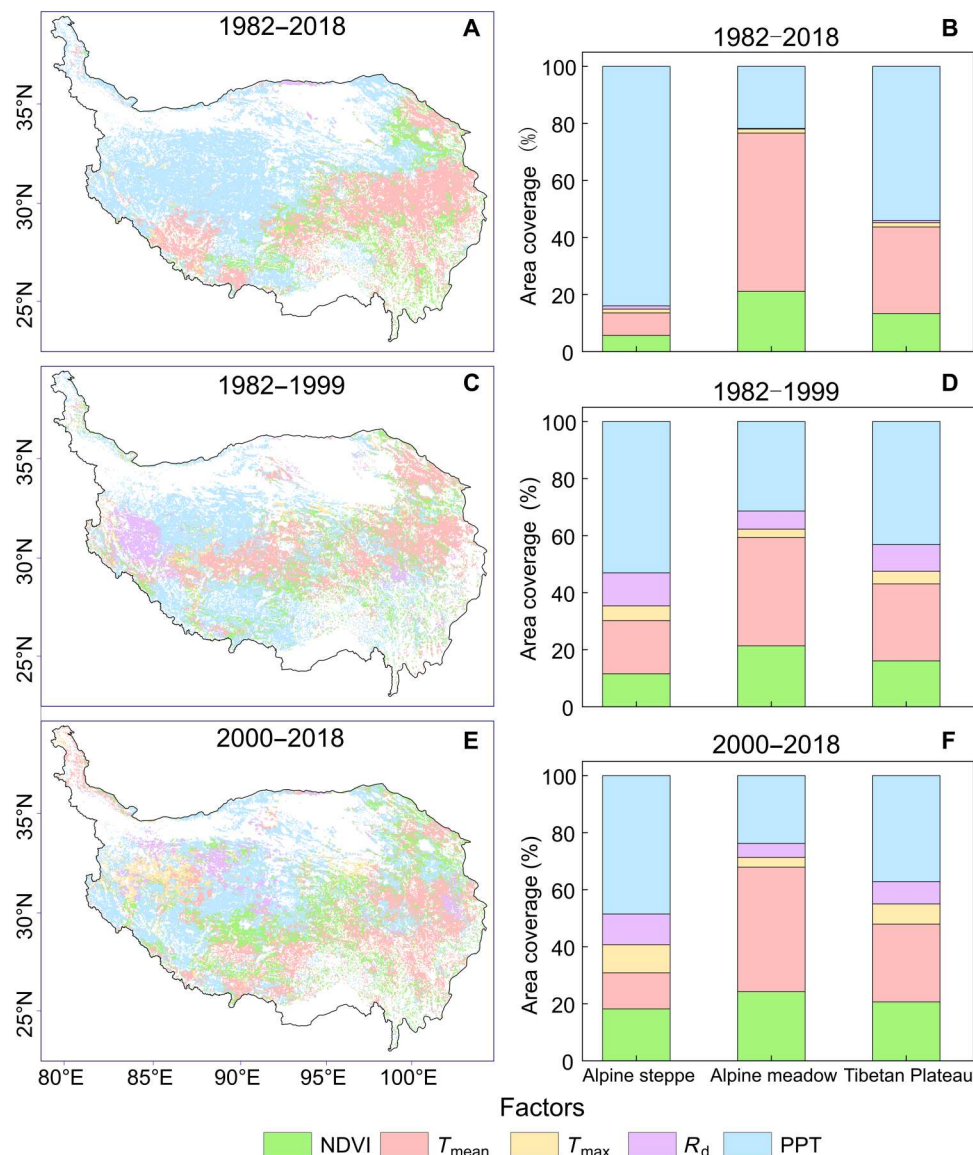
Fig. 4. Distribution of the dominant variables to the NEE trends and the proportion of the contribution of each variable over the different regions during different periods. (**A** and **B**) The 1982–2018 period. (**C** and **D**) The 1982–1999 period. (**E** and **F**) The 2000–2018 period. TP in (B), (D), and (F) consists of both alpine steppe and alpine meadow.

B, and 6, A and B). For the alpine meadow region, annual mean temperature and precipitation explained 68 and 49% of the NEE variation, respectively (Figs. 5, C and D, and 6, C and D), indicating the prominent effects of temperature on the NEE variability of the alpine meadow region. For the alpine steppe regions, precipitation (87%) explained a much larger portion of the NEE variations than temperature (38%), and this indicated the importance of water availability on the interannual variability of NEE in water-limited regions (Figs. 5, E and F, and 6, E and F). Consequently, these analyses further suggested that temperature and precipitation predominantly controlled the interannual variations in the NEE in alpine meadow and alpine steppe regions, respectively.

DISCUSSION

A warmer and wetter climate increased carbon sequestration in the alpine grasslands

Our study showed that the carbon sequestration capacity of the alpine grasslands on the TP increased markedly from 19.98 g C m^{-2} year^{-1} in 1982 to 49.86 g C m^{-2} year^{-1} in 2018 at a rate of 7.8 g C m^{-2} decade^{-1} on a per-unit area basis (i.e., from 29.26 to 73.01 Tg C year^{-1} with a rate of 11.4 Tg C decade^{-1} on a spatially integrated basis). The attribution analyses demonstrated that annual mean temperature and precipitation dominated the interannual variation of NEE in alpine grassland of the TP. Temperature and precipitation were the main factors regulating the NEE as in similar ecosystems (*10*, *28*, *29*). That is, the warming and wetting of the plateau enhanced the carbon sink intensity of the alpine habitats (Fig. 7). Warming enhanced plant growth and processes such
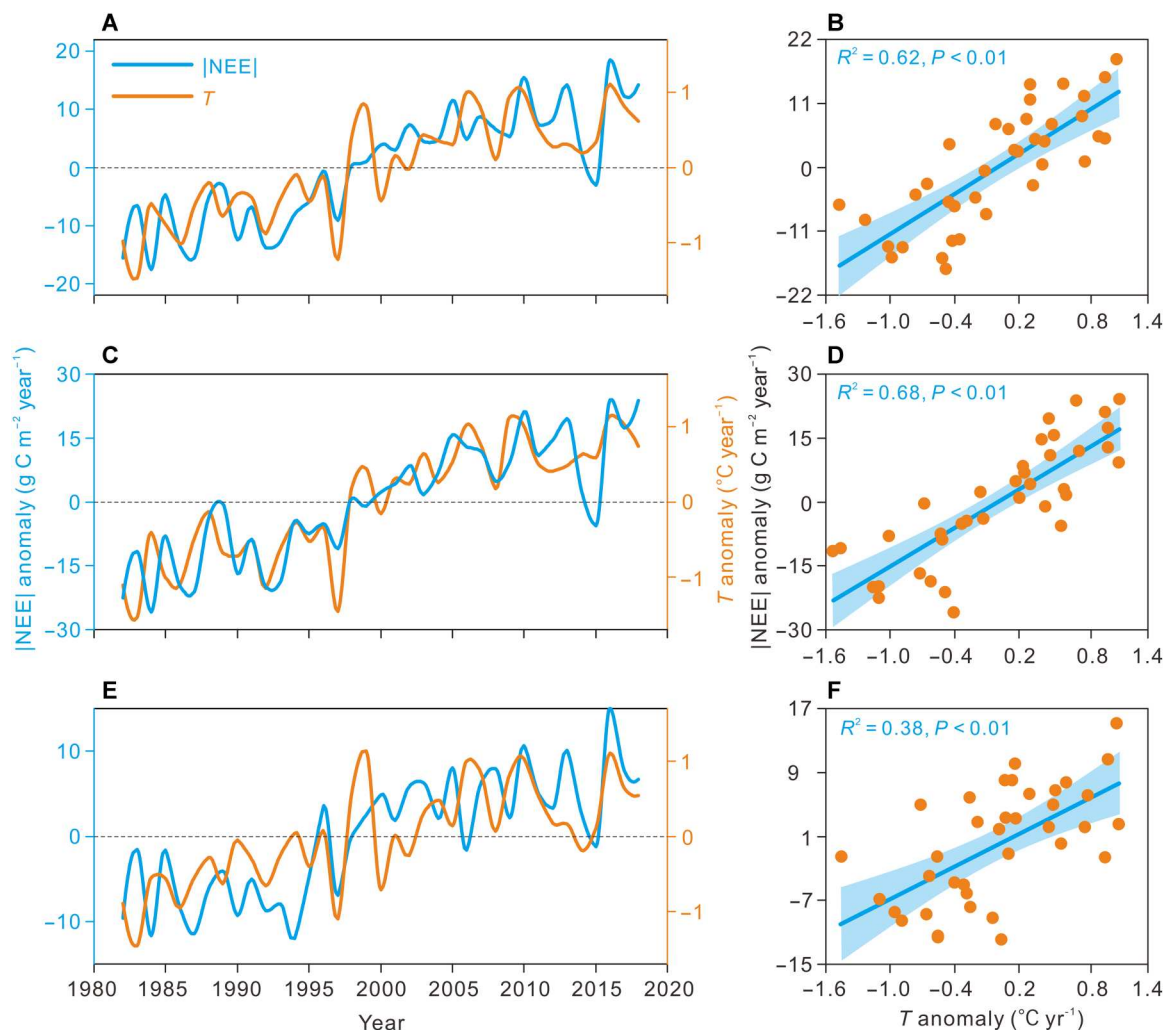
Fig. 5. Time series of and relationships between *T* and the NEE absolute value anomalies. *T*: annual mean air temperature. (**A** and **B**) Entire alpine grassland region of the TP. (**C** and **D**) Alpine meadow region. (**E** and **F**) Alpine steppe region. The solid lines in (B), (D), and (F) indicate the linear fit, while the blue shading represents the 95% confidence band of the fits.

as photosynthesis and transpiration, leading to a longer growing season (*30*, *31*). Enhanced photosynthesis and extended growing season increased gross carbon uptake (i.e., GPP) (*32*). Warming also boosted root and microbial activity and, hence, ecosystem respiration (*33*, *34*). However, plant dormancy outside the growing season led to a substantial CO_2 loss due to warming, reducing annual net carbon sequestration capacity (*35*). This was evidenced by the increase in NEE during winter and the decrease in summer (Fig. 2D). However, the overall higher carbon sequestration in this study suggests a larger increase in GPP than in ecosystem respiration. With rising air and soil temperature, atmospheric dryness and evapotranspiration will also increase, accelerating soil moisture decreases and water stress, adversely affecting carbon sequestration in water-limited regions. In other words, the effect of warming on net carbon sequestration in alpine grasslands is regulated by regional water supply (*25*). Therefore, warming made substantial contribution to the increase in net carbon sequestration in the wet alpine regions but had little effect in dry alpine steppes and even decreased

net carbon sequestration capacity in the desert steppe region in the northwest of the plateau (Fig. 3B1).

Precipitation outweighed other factors in the water-limited region and enhanced the net carbon sequestration capacity. Precipitation was more abundant on the eastern and southeastern parts of the plateau, and thus, the temperature was only a limiting factor for plant growth where water was nonlimiting (*15*, *27*, *36*). Therefore, the substantial warming of the alpine meadow region between 1982 and 2018 contributed to the marked decline in NEE (i.e., the enhanced carbon sink capacity) in the region. However, for the alpine steppes, soil moisture was a limiting factor of the vegetation growth, and increased precipitation made the soil environment moister, improved the supply of nutrients, promoted plant photosynthesis, and enhanced the carbon sequestration capacity (*37*). The relationship between precipitation and NEE directly reflected the impact of water availability on plant productivity in the alpine steppe regions. Precipitation was the dominant variable controlling the productivity and carbon sequestration of semiarid grasslands, which has been largely shown in previous studies (*28*, *29*, *38*).
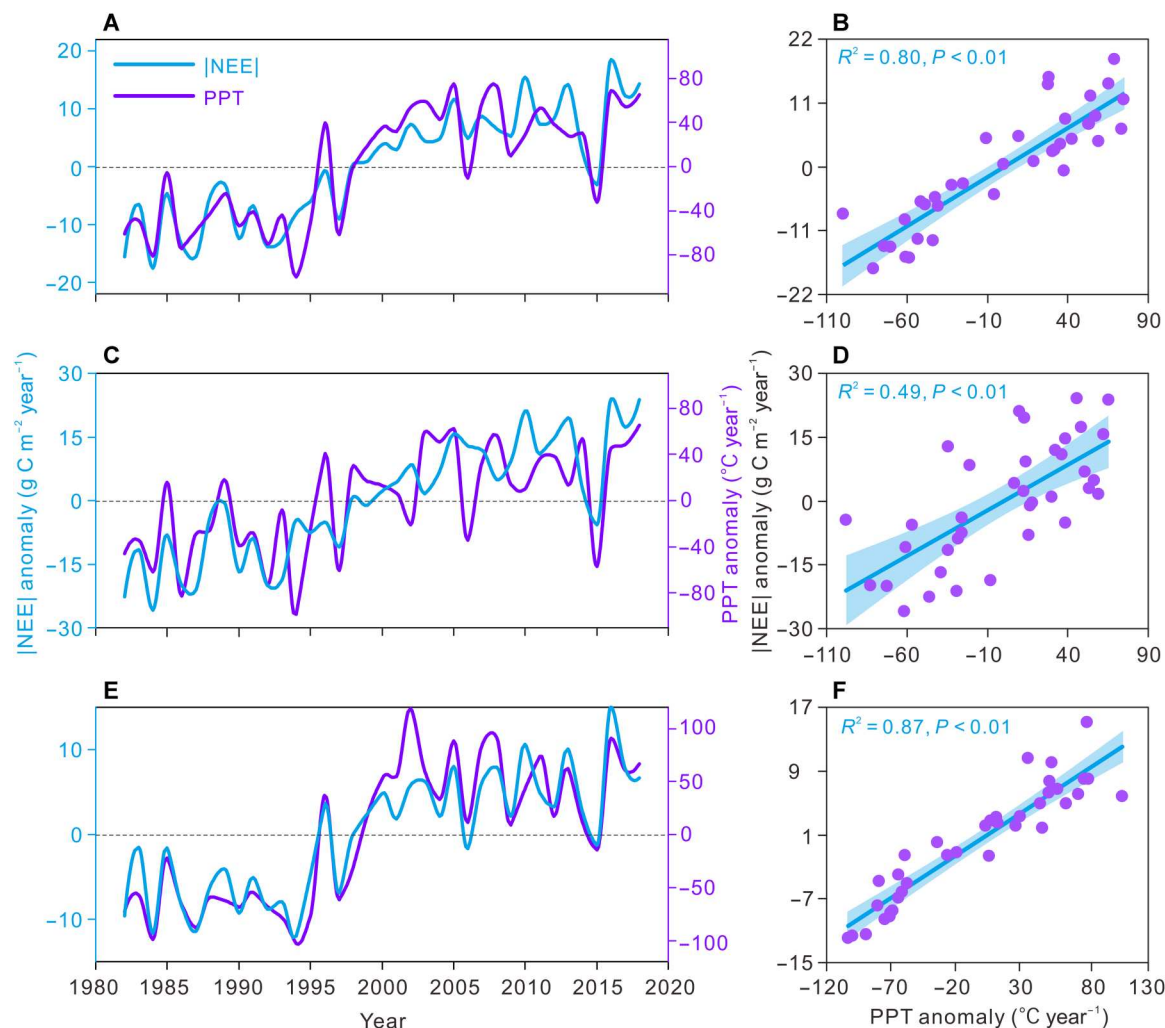
Fig. 6. Time series of and relationships between PPT and the NEE absolute value anomalies. PPT: annual precipitation. (**A** and **B**) Entire alpine grassland region of the TP. (**C** and **D**) Alpine meadow region. (**E** and **F**) Alpine steppe region. The solid lines in (B), (D), and (F) indicate the linear fit, while the blue shading represents the 95% confidence band of the fits.

The weakening of increasing carbon sequestration intensity in alpine grasslands on the TP from 2000 to 2018 was caused by the lack of water availability due to the decrease in precipitation from 2014 to 2015, and if the effects of these two years were excluded, the carbon sequestration intensity on the TP actually would have continuously enhanced (Fig. 1E). Moreover, warming and wetting could also contribute to net carbon sequestration in alpine grasslands through effects on biogeochemical cycling. For instance, warming can enhance soil nitrogen transformation rates and increasing precipitation can boost nitrogen availability, both of which can alleviate nitrogen limitation of alpine grassland (12).

In addition to warming and wetting, other factors such as nitrogen deposition, permafrost thawing, CO_2 fertilization effect, fencing, and grazing may also have altered carbon sources and sinks of alpine grasslands. Previous studies showed that nitrogen enrichment generally increases plant productivity and reduces or has negligible effect on ecosystem respiration (34, 39, 40), thus generally boosting ecosystem carbon sequestration. However, most of the nitrogen fertilization experiments were located in the eastern

alpine meadow region, and the resulting findings may not apply to alpine grasslands in other parts of the plateau. Actually, the nitrogen deposition on the TP is relatively low, so its enhancement effect on carbon sequestration in alpine grasslands is limited (12). Furthermore, as the largest alpine permafrost region in the middle latitudes, the TP alpine grassland region has huge soil organic carbon storage (20). The thawing of permafrost caused by warming will accelerate the release of carbon, which may weaken the carbon sink capacity of the TP (19). Moreover, rising atmospheric CO_2 can directly enhance net ecosystem carbon uptake by enhancing photosynthesis through CO_2 fertilization, which has been confirmed by the CO_2 enrichment experiment on the TP (41). Although the contribution of CO_2 fertilization can be quantified at the ecosystem scale through controlled experiments, its quantification at the regional scale requires scaling with modeling approaches and the simulations are often subject to large uncertainties mainly due to imperfect assumptions and uncertain parameters in the models. Meanwhile, grassland degradation due to increased grazing may also adversely affect the carbon sink potential of alpine
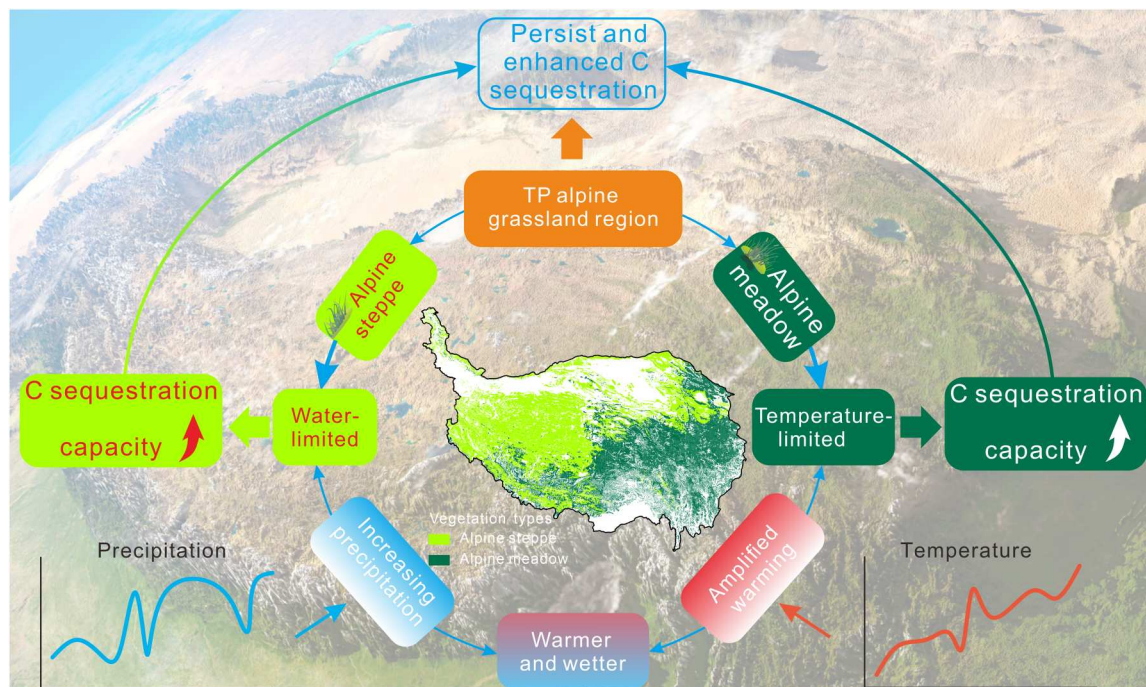
Fig. 7. Schematic diagram for the warmer and wetter climate increases the carbon sequestration capacity of the alpine grasslands.

grasslands. Therefore, the influences of these factors should be fully taken into account in future assessments of the carbon sequestration intensity in alpine grasslands on the TP.

Increasing in situ measurements improved the estimation of the carbon sequestration for the TP

Although an increasing number of studies have been conducted to quantify carbon sequestration of the TP at the regional scale using distinct methods, these carbon sequestration estimates still have large uncertainties (fig. S5). The large variability of the upscaled estimates was caused by various factors, such as ground flux data, model structure, and parameterization (*42*). The alpine grassland NEE for the TP from 2001 to 2015 extracted from different regional and global machine learning upscaling studies varied widely (fig. S6). Specifically, in some studies (fig. S6, B and D), the source-sink pattern of alpine grasslands did not match that of flux observations (*8, 43*). The remaining studies reported a gradual transition from a stronger carbon sink in the eastern alpine meadows to a weak carbon source or sink in the western alpine steppes, which could basically capture the spatial pattern of observation-based net carbon sequestration intensity in the alpine grasslands. The main reason for the large discrepancies among previous upscaling studies, ground-based observations, and our findings is that the performance of machine learning methods is greatly influenced by the availability and representativeness of training data, while previous synthesis and upscaling studies on the TP typically used NEE measurements from only a few flux sites (*3, 8, 43*). For example, Yao *et al.* (*3*) used five grassland sites, while other studies used only two sites. The NEE dataset developed in this study used observations from a much larger number of sites across the plateau that encompass various climate and vegetation types, which could increase

the accuracy of the carbon sequestration estimation for the alpine grasslands on the TP.

We also extracted the NEE estimates for the TP alpine grasslands from the global simulations based on eight terrestrial biosphere models over 1982–2010 from the Multi-scale Synthesis and Terrestrial Model Intercomparison Project (MsTMIP) (fig. S7). The spatial patterns of the NEE results of the diverse models exhibited substantial discrepancies and also had large differences from the observed NEE (*25*). These model simulations were conducted on a global scale, and key parameters were not calibrated for the TP. These models were based on imperfect assumptions and ecosystem processes, while model input data (e.g., climate and soil properties) also had substantial uncertainty. As a result, the model simulations have limited accuracy (*44*). What is more, we compared the NEE estimates for the alpine grassland region on the TP obtained using other process-based models (*21, 22, 26*). For example, one study used the Lund-Potsdam-Jena model to estimate the alpine grassland net ecosystem productivity on the TP from 1979 to 2005 with soil texture and CO_2 concentration data as the inputs and the observation flux data as the constraints. Their results showed that the annual mean NEP increased from approximately 36 g C m^{-2} year^{-1} in 1979 to more than 80 g C m^{-2} year^{-1} in 2005 (*26*). For the overlapping period, the estimates of the magnitude and trend in carbon sequestration of that study were much larger than those of our study likely because input datasets, model mechanisms, and model parameters were different. The data processing method used in the abovementioned research may have overestimated carbon sink on the TP (*45*). This also indicates that there is still a great deal of uncertainty in quantifying the alpine grassland NEE on the TP and that further research is urgently needed to reduce its uncertainties.

The results of this study may also be subject to various sources of uncertainty. First, the observations from all the sites used in this study were concentrated in 2002–2018, and the training of the model was therefore limited to this period. Because of the lack of observations before 2002, the gridded NEE estimates from 1982 to 2001 may have larger uncertainty. However, we analyzed the probability density distribution of regional mean temperature and precipitation during 1982–2001 and 2002–2018 and found that there was a high degree of overlap between the two periods (fig. S8). This indicates that the training data of the latter period could capture the climatic conditions of the previous period fairly well and that the model developed with data for 2002–2018 could be used to estimate NEE for 1982–2001. Many previous studies also used machine learning models trained with data from one period to estimate carbon and/or water fluxes for another period (*42*, *46–47*). In addition, although machine learning–based methods are widely used in upscaling estimation of regional carbon fluxes and their upscaling results are often used as benchmarks for process-based models, the representativeness of flux sites and the inadequate selection of explanatory variables will cause uncertainty in regional NEE estimations (*3*, *8*). For example, the 25 alpine grassland sites used in this study were mainly located in the alpine meadow region on the eastern and central parts of the plateau, and there is a lack of observation sites on the western part of the plateau. Thus, the NEE estimation for the alpine steppe region may have certain uncertainty. Moreover, the explanatory variables applied in this study may not be sufficient to adequately capture the changes in the NEE. Despite the various sources of uncertainty, our gridded NEE estimates had reasonable accuracy (figs. S9 to S11) and the uncertainty (as measured by SD) of the annual NEE was relatively low (fig. S12). Although the changes in the NEE on the monthly scale are closely related to precipitation, temperature, radiation, vegetation greenness, and canopy development, they are also closely linked to other factors such as topsoil water content, nitrogen deposition, fencing, grazing, and above/subsurface biomass that were not considered (*34*, *48*). For some of the variables (e.g., fencing and grazing), regional-scale data are not yet available for the TP; for the variables having data available for the TP, the data tend to have large uncertainties and very coarse spatial resolutions, and they might only be available for part of our study period (*49*, *50*).

Besides the "bottom-up" upscaling estimates based on flux observations, the "top-down" atmospheric inversion methods are also admittedly indispensable tools (*51*). There are mounting satellite sensors and platforms, such as OCO-3 and GOSAT, that can observe the atmospheric CO_2 vertical column concentration. The combination of these satellite data with increasingly sophisticated atmospheric inversion methods may lead to more accurate NEE estimation than previous inversion efforts. The NEE estimates based on inversion methods and those resulting from bottom-up upscaling methods and ground-based flux observations can be compared against each other, which can potentially improve the future estimation of carbon sink capacity in the alpine grasslands of the TP. In addition, with the increase of government investment in the study of the TP and the implementation of some major scientific research projects (e.g., the Second Tibetan Plateau Scientific Expedition and Research program), there will be a growing number of ground flux observation sites on the plateau (*52*). Moreover, besides the sites that we used, there are a number of existing flux sites on the TP that the flux observations are not yet publicly

available. The growing number of flux sites and increasing awareness of data sharing among researchers will likely allow us to better quantify the carbon sink capacity of the alpine grasslands on the TP in the future.

Implications and outlook
Accurately estimating the carbon sequestration of the alpine grasslands on the TP is crucial to understanding their role in regional and global carbon cycles and has prominent implication for future projections of carbon-climate feedbacks. On the basis of our upscaled estimation, the amount of carbon that the alpine grasslands on the TP sequestrated ranged from 18.02 to 54.08 g C m^{-2} year^{-1} (i.e., from 26.39 to 79.19 Tg C year^{-1}) with an average of 35.59 ± 9.90 g C m^{-2} year^{-1} (i.e., 52.11 ± 14.50 Tg C year^{-1}) during 1982–2018. In general, the alpine grassland region on the TP is an important carbon sink. Our upscaling method did not explicitly consider factors such as grassland grazing (*53*), aquatic carbon export (*54*), and fire emissions. If these factors were taken into account, the carbon sequestration capacity of the alpine grasslands on the TP could be lower. Moreover, warming and increased precipitation dominated the enhancement of carbon sequestration intensity in alpine meadows and alpine steppes, respectively. Warmer and wetter climate is projected to continue on the TP, and thus, the increasing trend of carbon sinks in alpine grasslands is likely to be maintained. Further, it is known that the TP is the largest alpine permafrost region in the world, and the permafrost is basically located in the alpine grassland area (*20*). The rising temperatures on the TP in recent decades have led to the thawing of the permafrost and thickening of the active layer, which may have accelerated the release of the carbon stored in the permafrost (*19*). Our research shows that the carbon sequestration capacity of the alpine grasslands on the TP has been enhanced by a warmer and wetter climate. This indicates that, annually, the carbon input is still greater than the carbon output in the alpine grassland region of the TP. However, if the temperature continues to rise in the future, the melting of the permafrost is likely to accelerate, and the amount of carbon released may increase, which might weaken the carbon sink capacity of alpine grasslands on the TP.

MATERIALS AND METHODS
Dataset
Collection of eddy covariance flux data
In total, data from 25 carbon flux observation sites on the TP were obtained in this study (Fig. 1A and table S1). These sites covered most of the typical grassland ecosystem types in the region: alpine *Kobreia* meadow (11 sites), alpine swamp meadow (6 sites), alpine shrub meadow (2 sites), and alpine steppe (6 sites, of which NMC, DX, QM, and ND66 were alpine meadow steppes, and NASDE and Muztagh were alpine desert steppes). Most of these flux observation sites were located in the central and eastern parts of the TP, and there were fewer sites in the western and northern parts of the plateau, especially in regions such as the Qiangtang Plateau, due to the harsh environment and lack of convenient roads.

A total of 107 site-year of data from all of the sites combined were acquired in this study, with an average of 4.3 years of data per site. These site data can be divided into three types: (i) raw 10-Hz data available; (ii) 30-min data acquired using flux processing software; and (iii) daily data obtained from the literature. Specifically, the data

from NMC, Muztagh, NASDE, QM_a, and QM_b belonged to type 1. At these sites, the eddy covariance instruments were set up and maintained by the Institute of Tibetan Plateau Research, Chinese Academy of Sciences. The data from AR, MQ, HLG, BJ, AD, NPAM, YK, JYL, DSL, LB, ND66, Haibei_a, and Haibei_b belonged to type 2, and most of these data were downloaded from the Big Earth Data Platform for Three Poles (https://poles.tpdc.ac.cn/en/). The data from sites GL (55), NQ (38), REG (56), SZ (57), Haibei-c, DX_a, and DX_b belonged to type 3. The data for Haibei-c and DX-a were downloaded from the official website of ChinaFlux (http://chinaflux.org/enn/). For the sites with type 1 data, standardized procedures were adopted to process the raw 10-Hz data to 30-min carbon flux data. Furthermore, to obtain the daily and monthly integrated data, we used the R-based package (REddyProc) developed by the Max Planck Institute for Biogeochemistry to fill in the gaps in the half-hour NEE for the type 1 and 2 data (58). In total, 1223 site-month flux data were used to construct the machine learning model for the development of the TP alpine grassland NEE dataset.

Satellite and climate input datasets

The NEE is the synergistic result of photosynthesis and respiration and is influenced by a variety of biological, atmospheric, hydrological, and soil factors (2). At the ecosystem scale, the GPP is mainly affected by environmental factors, such as solar radiation, air temperature, vapor pressure deficit, and water availability, and biological factors, such as canopy development and phenology. Ecosystem respiration consists of autotrophic and heterotrophic respiration, with soil respiration accounting for the largest proportion. Ecosystem respiration is closely related to plant photosynthesis, metabolism, and litterfall. Specifically, autotrophic respiration can be expressed empirically as a function of the air temperature and GPP, while heterotrophic respiration is usually modeled as a function of the soil temperature and moisture and the substrate (59). It is obvious that these variables affect the NEE either directly or indirectly, and many of these variables can be assessed using satellite remote sensing and reanalysis data. For example, the normalized difference vegetation index (NDVI) and the enhanced vegetation index (EVI) are biophysical indicators of vegetation canopy development, phenology, and greenness, and they are closely related to the photosynthetic intensity of the vegetation and seasonal changes in the biomass. In contrast to remote sensing vegetation indices, which can better reflect the greenness of vegetation, the sun-induced chlorophyll fluorescence (SIF) is considered to be an indicator of the actual photosynthetic function of plants. Previous studies have also revealed the notable relationship between the SIF and photosynthesis at the ecosystem scale (60).

Therefore, in this study, the temperature, precipitation, radiation, NDVI, EVI, and SIF, which are strongly correlated with ecosystem carbon fluxes, were mainly selected as the explanatory variables for the NEE upscaling simulation. The moderate-resolution imaging spectroradiometer (MODIS) 16-day composite NDVI and EVI products (MOD13Q1) with a 250-m spatial resolution from 2000 to 2018 were used in this study (https://search.earthdata.nasa.gov/). The original 16-day NDVI and EVI data were first aggregated to monthly intervals using a maximum value composition approach and then were resampled to a 1-km resolution. Moreover, the advanced very high-resolution radiometer version 6 (AVHRR-V6) NDVI products with a 0.05° × 0.05° spatial resolution and a daily temporal resolution collected by the AVHRR sensors were used (https://ncei.noaa.gov/products/

climate-data-records/normalized-difference-vegetation-index). To minimize the atmospheric and cloud pollution effects, we used the monthly maximum synthesis to calculate the monthly scale NDVI datasets. It has been verified that the monthly AVHRR NDVI and MODIS-NDVI are basically consistent over the TP, exhibiting good reliability. In addition, monthly SIF data used in this study were obtained from the Earth System Research Center at the University of New Hampshire, USA (http://data.globalecology.unh.edu/data/GOSIF_v2/). The regional-scale gridded reanalysis meteorological datasets, including air temperature, precipitation, and downward shortwave radiation, were derived from the China Meteorological Forcing Dataset (61). The dataset has a temporal resolution of daily scale and a spatial resolution of 0.1° × 0.1°. In this study, daily-scale meteorological data were aggregated to monthly-scale data, including monthly mean temperature (T_{mean}), monthly mean downward shortwave radiation (R_d), monthly maximum temperature (T_{max}), and monthly cumulative precipitation (PPT). To match the spatial resolution of the two NDVI datasets described in the previous section, we resampled the regional-scale meteorological data to a resolution of 1 km and 0.05°, respectively.

Independent NEE datasets

In this study, besides the gridded NEE data that we generated by upscaling flux observations to the regional scale, six existing regional NEE datasets developed by previous studies via upscaling and based on different machine learning methods were also used. The regional results for the TP were extracted from these independent datasets and were compared with the upscaled results in this study. Specifically, Yao et al. (3) created a regional NEE dataset for China based on carbon flux observations from 46 flux sites (5 sites on the TP) combined with remote sensing and reanalysis data using the model tree ensemble method. Zeng et al. (43) created a global carbon flux dataset based on the FLUXNET 2015 dataset and other data using the random forest (RF) method to obtain a global carbon flux dataset. The remaining four datasets were the FluxCom datasets of the global carbon fluxes created by Jung et al. (8) based on the upscaling of 224 flux sites from FLUXNET. Among them, MTE (RS) was obtained entirely from remotely sensed data using a model tree ensemble approach, while the remaining three were obtained from remotely sensed data with reanalyzed meteorological data (CRU JRA) driven by multivariate adaptive regression splines, RF, and artificial neural networks. In addition, in this study, the NEE results were also compared with the model simulations from the MsTMIP (https://daac.ornl.gov/cgi-bin/dsviewer.pl?ds_id=1225). The MsTMIP dataset provides global gridded estimates of the carbon fluxes between the land and atmosphere for 15 terrestrial biosphere models in a standard format. The temporal and spatial resolutions of the data are monthly and 0.5°, and the time span is 1982–2010 (44). The dataset of the MsTMIP simulations (BIOME-BGC, CLASS-CTEM-N, CLM4, CLM4VIC, DLEM, ISAM, TEM, and TRIPLEX-GHG) was divided into five categories based on the changes in the climate driving variables, land use data, and CO_2 and nitrogen deposition, of which the BG1 simulations were selected for use in this study.

Construction of monthly regional NEE estimation model

Considering the differences in the availability of the MODIS higher-resolution (1 km) remote sensing data from 2000 to 2018 and the AVHRR NDVI lower-resolution remote (0.5°) sensing data from

1982 to 2018, we used two groups of explanatory variables for the model development and the estimation of the regional NEE (table S2). Moreover, the simulation involving the shorter-term (2000–2018) higher-resolution MODIS NDVI and EVI data was referred to as case 1, while the simulation involving the longer-term (1982–2018) lower-resolution AVHRR NDVI was referred to as case 2 (table S2). Since case 1 adopted more variables with higher-resolution (1 km; e.g., NDVI, EVI, and SIF) data, the regional NEE obtained by case 1 following upscaling might have better reliability. Thus, the higher-resolution, shorter-term regional NEE dataset can be used as a comparison benchmark for the longer-term regional NEE dataset, while the longer-term regional NEE can be further used to analyze the spatial and temporal patterns and driving factors of NEE for alpine grasslands on the TP. Further, in this study, we applied regression-based machine learning approaches to upscale the flux NEE measurements. In this study, four machine learning methods were selected: the support vector regression (SVR) (*7*), RF regression (*62*), ETR (*63*), and extreme gradient boosting (XGBoost) (*64*) methods, which have been widely used in previous regional upscaling studies. First, the site observed NEE data and the explanatory variables corresponding to the site grid were randomly divided into two groups: 70% of the data (884 site months) were used as the training dataset, and the remaining 30% (380 site months) were used as the testing dataset (mainly to test the performance of the trained model). For the training dataset, the parameters of the machine learning model were optimized and selected using the *k*-fold cross-validation and grid search method. The specific process was as follows. We randomly and equally divided the training dataset into *k* parts. In each parameter grid search process, (*k* − 1) parts of the data were used as training data, and the *k*th part of the data was used as validation data. The training was repeated *k* times in turn to ensure that each part of the data was involved in the training and validation. Then, *k* training model metrics were obtained, and the average of these *k* metrics was the *k* times cross-validation of the model metrics. Although *k*-fold cross-validation takes a long time in practical applications, the data are fully used. The mean absolute error (MAE), RMSE, and correlation coefficient (R^2) were used to evaluate the performance of each model

$$R^2 = \frac{\sum_{i=1}^{n}(E_i - \overline{O_i})^2}{\sum_{i=1}^{n}(O_i - \overline{O_i})^2} \tag{1}$$

$$\text{RMSE} = \sqrt{\frac{1}{n}\sum_{i=1}^{n}(E_i - O_i)^2} \tag{2}$$

$$\text{MAE} = \frac{1}{n}\sum_{i=1}^{n}|E_i - O_i| \tag{3}$$

In Eqs. 1 to 3, E_i is the monthly NEE simulated by the models and O_i is the measured monthly NEE. We chose the model with the smallest MAE and RMSE and the largest R^2 as the best model. The four machine learning methods (ETR, RF, SVR, and XGBoost) basically have the same model configuration process. However, the SVR method needs to standardize the input data because the

different dimensions of the data will affect the division of the hyperplane, while the other methods with decision trees as the basic structure have only small differences. In terms of the model application, the monthly NEE of the alpine grassland region on the TP was generated using the trained model and the regional explanatory variables presented in table S2 (the results of the two cases with spatial resolutions of 1 km and 0.05°).

Performance of the regression machine learning methods

We used the regression machine learning method to construct data-driven models at the site scale during the training process, and observation data were used to constrain the model parameters. Then, the training results of the models were verified using the testing data. Case 1 involved shorter-term (2000–2018) and higher-resolution (1 km) variables, while case 2 involved longer-term (1982–2018) and lower-resolution (0.05°) variables. The training and testing results of case 1 are shown in figs. S9 and S10. The training results of the four machine learning methods show that the ETR, RF, and XGBoost methods were close in terms of accuracy and that they all outperformed the SVR method (fig. S9). The test results show that the accuracies of the four methods were not very different, with the ETR method (MAE = 0.34, RMSE = 0.51, R^2 = 0.75) performing slightly better than the other three methods (fig. S10). Therefore, on the basis of the assessment results of the above-mentioned models, we used the ETR method for the estimation of the monthly-scale NEE of the TP alpine grassland during 2000–2018 on a per-pixel basis using the explanatory variables for case 1. For case 2, we also used the ETR method to train and test the observed NEE and the relevant explanatory variables to facilitate the comparison and analysis of the regional upscaling results with case 1. Since there were fewer explanatory variables in case 2 than in case 1, the performance of case 2 was somewhat lower than that of case 1 for both the training (MAE = 0.26, RMSE = 0.37, R^2 = 0.85) and testing results (MAE = 0.34, RMSE = 0.54, R^2 = 0.72), but the difference was not large (fig. S11). Then, the monthly-scale NEE of the alpine grassland region on the TP during 1982–2018 was estimated on a per-pixel basis using the explanatory variables associated with the ETR optimal model trained in case 2.

Analysis methods

In this study, the attribution analysis of the contribution of each driving variable to the changes in the trend of the NEE was based on the upscaling results obtained for case 2. The driving factors of the NEE included the PPT, NDVI, R_d, T_{mean}, and T_{max}. A control experiment (Expert_CON) and sensitivity experiment (Expert_SEN) were set to attribute the regional interannual variation trend of the NEE. Taking 1982–2018 as an example, the actual values of each explanatory variable in the control experiment remained unchanged during 1982–2018, and five sensitivity experiments were conducted on the explanatory variables, namely, exper_PPT, exper_NDVI, exper_R_d, exper_T_{mean}, and exper_T_{max}. In each sensitivity test, the measured explanatory variables were kept constant at their mean values from 1982 to 2018, and the other variables were kept the same as in the control test. The difference in the NEE trends of the control test and the sensitivity test was considered to be the contribution of this explanatory variable to the NEE trend. However, there are interactions between these drivers, which may introduce some uncertainty into the estimation of each factor's individual contribution to the change in the NEE.

Therefore, in this study, the separation method proposed by Sun *et al.* (*65*) was used, which can minimize the error caused by the interactions between the explanatory variables and has been better applied in several studies (*66, 67*)

$$\sum_{k \neq i}^{n} C_k = E_{\text{exper\_}i} \tag{4}$$

where $\sum_{k \neq i}^{n} C_k$ is the total contribution of all the remaining explanatory variables to the NEE trend of the control experiment, except the ith factor; C_k is the contribution of the kth factor to the NEE trend; n is the number of sensitivity experiments ($n = 5$ in this study); and $E_{\text{exper\_}i}$ is the NEE trend of each sensitivity experiment. By solving the abovementioned equations, we can obtain the contribution of each driver to the NEE trend C_i

$$C_i = \frac{\sum_{k \neq i}^{n} E_{\text{exper\_}k} - (n-2) \cdot E_{\text{exper\_}i}}{n-1} \tag{5}$$

Similarly, following the same analysis for 1982–2018, we also analyzed the contribution of each explanatory variable to the trend of the NEE during the two time periods of 1982–1999 and 2000–2018. The Mann-Kendall test is a nonparametric trend test method that has been widely used in hydrometeorological time series analysis. Compared with the linear regression method, it can provide a more accurate estimation of the skewness of the data (*68*). The Theil-Sen method was used to calculate the magnitude of the trend, and the nonparametric Mann-Kendall method was used to determine the level of significance of the interannual trends in the NEE and climate variables.

Supplementary Materials

This PDF file includes:
Figs. S1 to S12
Tables S1 and S2

View/request a protocol for this paper from *Bio-protocol*.

REFERENCES AND NOTES

1. P. Friedlingstein, M. O'Sullivan, M. W. Jones, R. M. Andrew, L. Gregor, J. Hauck, C. Le Quéré, I. T. Luijkx, A. Olsen, G. P. Peters, W. Peters, J. Pongratz, C. Schwingshackl, S. Sitch, J. G. Canadell, P. Ciais, R. B. Jackson, S. R. Alin, R. Alkama, A. Arneth, V. K. Arora, N. R. Bates, M. Becker, N. Bellouin, H. C. Bittig, L. Bopp, F. Chevallier, L. P. Chini, W. Evans, S. Falk, R. A. Feely, T. Gasser, M. Gehlen, T. Gkritzalis, L. Gloege, G. Grassi, N. Gruber, Ö. Gürses, I. Harris, M. Hefner, R. A. Houghton, G. C. Hurtt, Y. Iida, T. Ilyina, A. K. Jain, A. Jersild, K. Kadono, E. Kato, D. Kennedy, K. K. Goldewijk, J. Knauer, J. I. Korsbakken, P. Landschützer, N. Lefèvre, K. Lindsay, J. Liu, Z. Liu, G. Marland, N. Mayot, M. J. McGrath, N. Metzl, N. M. Monacci, D. R. Munro, S.-I. Nakaoka, Y. Niwa, K. O'Brien, T. Ono, P. I. Palmer, N. Pan, D. Pierrot, K. Pocock, B. Poulter, L. Resplandy, E. Robertson, C. Rödenbeck, C. Rodriguez, T. M. Rosan, J. Schwinger, R. Séférian, J. D. Shutler, I. Skjelvan, T. Steinhoff, Q. Sun, A. J. Sutton, C. Sweeney, S. Takao, T. Tanhua, P. P. Tans, X. Tian, H. Tian, B. Tilbrook, H. Tsujino, F. Tubiello, G. R. van der Werf, A. P. Walker, R. Wanninkhof, C. Whitehead, A. W. Wranne, R. Wright, W. Yuan, C. Yue, X. Yue, S. Zaehle, J. Zeng, B. Zheng, Global carbon budget 2022. *Earth Syst. Sci. Data* **14**, 4811–4900 (2022).

2. J. Xiao, Q. Zhuang, D. D. Baldocchi, B. E. Law, A. D. Richardson, J. Chen, R. Oren, G. Starr, A. Noormets, S. Ma, S. B. Verma, S. Wharton, S. C. Wofsy, P. V. Bolstad, S. P. Burns, D. R. Cook, P. S. Curtis, B. G. Drake, M. Falk, M. L. Fischer, D. R. Foster, L. Gu, J. L. Hadley, D. Y. Hollinger, G. G. Katul, M. Litvak, T. A. Martin, R. Matamala, S. McNulty, T. P. Meyers, R. K. Monson, J. W. Munger, W. C. Oechel, K. T. Paw U, H. P. Schmid, R. L. Scott, G. Sun, A. E. Suyker, M. S. Torn, Estimation of net ecosystem carbon exchange for the conterminous United States by combining MODIS and AmeriFlux data. *Agric. For. Meteorol.* **148**, 1827–1847 (2008).

3. Y. Yao, Z. Li, T. Wang, A. Chen, X. Wang, M. Du, G. Jia, Y. Li, H. Li, W. Luo, Y. Ma, Y. Tang, H. Wang, Z. Wu, J. Yan, X. Zhang, Y. Zhang, Y. Zhang, G. Zhou, S. Piao, A new estimation of China's net ecosystem productivity based on eddy covariance measurements and a model tree ensemble approach. *Agric. For. Meteorol.* **253-254**, 84–93 (2018).

4. J. Xiao, F. Chevallier, C. Gomez, L. Guanter, J. A. Hicke, A. R. Huete, K. Ichii, W. Ni, Y. Pang, A. F. Rahman, G. Sun, W. Yuan, L. Zhang, X. Zhang, Remote sensing of the terrestrial carbon cycle: A review of advances over 50 years. *Remote Sens. Environ.* **233**, 111383 (2019).

5. S. Sitch, C. Huntingford, N. Gedney, P. E. Levy, M. Lomas, S. L. Piao, R. Betts, P. Ciais, P. Cox, P. Friedlingstein, C. D. Jones, I. C. Prentice, F. I. Woodward, Evaluation of the terrestrial carbon cycle, future plant geography and climate-carbon cycle feedbacks using five Dynamic Global Vegetation Models (DGVMs). *Glob. Chang. Biol.* **14**, 2015–2039 (2008).

6. M. Jung, M. Reichstein, H. A. Margolis, A. Cescatti, A. D. Richardson, M. A. Arain, A. Arneth, C. Bernhofer, D. Bonal, J. Chen, D. Gianelle, N. Gobron, G. Kiely, W. Kutsch, G. Lasslop, B. E. Law, A. Lindroth, L. Merbold, L. Montagnani, E. J. Moors, D. Papale, M. Sottocornola, F. Vaccari, C. Williams, Global patterns of land-atmosphere fluxes of carbon dioxide, latent heat, and sensible heat derived from eddy covariance, satellite, and meteorological observations. *J. Geophys. Res.* **116**, G00J07 (2011).

7. K. Ichii, M. Ueyama, M. Kondo, N. Saigusa, J. Kim, M. C. Alberto, J. Ardö, E. S. Euskirchen, M. Kang, T. Hirano, J. Joiner, H. Kobayashi, L. B. Marchesini, L. Merbold, A. Miyata, T. M. Saitoh, K. Takagi, A. Varlagin, M. S. Bret-Harte, K. Kitamura, Y. Kosugi, A. Kotani, K. Kumar, S. G. Li, T. Machimura, Y. Matsuura, Y. Mizoguchi, T. Ohta, S. Mukherjee, Y. Yanagi, Y. Yasuda, Y. Zhang, F. Zhao, New data-driven estimation of terrestrial CO_2 fluxes in Asia using a standardized database of eddy covariance measurements, remote sensing data, and support vector regression. *J. Geophys. Res. Biogeo.* **122**, 767–795 (2017).

8. M. Jung, C. Schwalm, M. Migliavacca, S. Walther, G. Camps-Valls, S. Koirala, P. Anthoni, S. Besnard, P. Bodesheim, N. Carvalhais, F. Chevallier, F. Gans, D. S. Goll, V. Haverd, P. Köhler, K. Ichii, A. K. Jain, J. Liu, D. Lombardozzi, J. E. M. S. Nabel, J. A. Nelson, M. O'Sullivan, M. Pallandt, D. Papale, W. Peters, J. Pongratz, C. Rödenbeck, S. Sitch, G. Tramontana, A. Walker, U. Weber, M. Reichstein, Scaling carbon fluxes from eddy covariance sites to globe: Synthesis and evaluation of the FLUXCOM approach. *Biogeosciences* **17**, 1343–1365 (2020).

9. A.-M. Virkkala, J. Aalto, B. M. Rogers, T. Tagesson, C. C. Treat, S. M. Natali, J. D. Watts, S. Potter, A. Lehtonen, M. Mauritz, E. A. G. Schuur, J. Kochendorfer, D. Zona, W. Oechel, H. Kobayashi, E. Humphreys, M. Goeckede, H. Iwata, P. M. Lafleur, E. S. Euskirchen, S. Bokhorst, M. Marushchak, P. J. Martikainen, B. Elberling, C. Voigt, C. Biasi, O. Sonnentag, F. W. Parmentier, M. Ueyama, G. Celis, V. L. St Louis, C. A. Emmerton, M. Peichl, J. Chi, J. Jarveoja, M. B. Nilsson, S. F. Oberbauer, M. S. Torn, S. J. Park, H. Dolman, I. Mammarella, N. Chae, R. Poyatos, E. Lopez-Blanco, T. R. Christensen, M. J. Kwon, T. Sachs, D. Holl, M. Luoto, Statistical upscaling of ecosystem CO_2 fluxes across the terrestrial tundra and boreal domain: Regional patterns and uncertainties. *Glob. Chang. Biol.* **27**, 4040–4059 (2021).

10. L. Zhang, H. Guo, G. Jia, B. Wylie, T. Gilmanov, D. Howard, L. Ji, J. Xiao, J. Li, W. Yuan, T. Zhao, S. Chen, G. Zhou, T. Kato, Net ecosystem productivity of temperate grasslands in northern China: An upscaling study. *Agric. For. Meteorol.* **184**, 71–81 (2014).

11. J. Qiu, China: The third pole. *Nature* **454**, 393–396 (2008).

12. H. Chen, P. Ju, Q. Zhu, X. Xu, N. Wu, Y. Gao, X. Feng, J. Tian, S. Niu, Y. Zhang, C. Peng, Y. Wang, Carbon and nitrogen cycling on the Qinghai–Tibetan Plateau. *Nat. Rev. Earth Environ.* **3**, 701–716 (2022).

13. Y. Wang, W. Lv, K. Xue, S. Wang, L. Zhang, R. Hu, H. Zeng, X. Xu, Y. Li, L. Jiang, Y. Hao, J. Du, J. Sun, T. Dorji, S. Piao, C. Wang, C. Luo, Z. Zhang, X. Chang, M. Zhang, Y. Hu, T. Wu, J. Wang, B. Li, P. Liu, Y. Zhou, A. Wang, S. Dong, X. Zhang, Q. Gao, H. Zhou, M. Shen, A. Wilkes, G. Miehe, X. Zhao, H. Niu, Grassland changes and adaptive management on the Qinghai–Tibetan Plateau. *Nat. Rev. Earth Environ.* **3**, 668–683 (2022).

14. S. Liu, K. Zamanian, P.-M. Schleuss, M. Zarebanadkouki, Y. Kuzyakov, Degradation of Tibetan grasslands: Consequences for carbon and nutrient cycles. *Agric. Ecosyst. Environ.* **252**, 93–104 (2018).

15. T. Yao, Y. Xue, D. Chen, F. Chen, L. Thompson, P. Cui, T. Koike, W. K. M. Lau, D. Lettenmaier, V. Mosbrugger, R. Zhang, B. Xu, J. Dozier, T. Gillespie, Y. Gu, S. Kang, S. Piao, S. Sugimoto, K. Ueno, L. Wang, W. Wang, F. Zhang, Y. Sheng, W. Guo, Ailikun, X. Yang, Y. Ma, S. S. P. Shen, Z. Su, F. Chen, S. Liang, Y. Liu, V. P. Singh, K. Yang, D. Yang, X. Zhao, Y. Qian, Y. Zhang, Q. Li, Recent third pole's rapid warming accompanies cryospheric melt and water cycle intensification and interactions between monsoon and environment: Multidisciplinary approach with observations, modeling, and analysis. *Bull. Am. Meteorol. Soc.* **100**, 423–444 (2019).

16. Q. You, Z. Cai, N. Pepin, D. Chen, B. Ahrens, Z. Jiang, F. Wu, S. Kang, R. Zhang, T. Wu, P. Wang, M. Li, Z. Zuo, Y. Gao, P. Zhai, Y. Zhang, Warming amplification over the arctic pole and third pole: Trends, mechanisms and consequences. *Earth Sci. Rev.* **217**, 103625 (2021).

17. J. Sun, E. Liang, I. C. Barrio, J. Chen, J. Wang, B. Fu, Fences undermine biodiversity targets. *Science* **374**, 269 (2021).

18. D. Kou, G. Yang, F. Li, X. Feng, D. Zhang, C. Mao, Q. Zhang, Y. Peng, C. Ji, Q. Zhu, Y. Fang, X. Liu, Xu-Ri, S. Li, J. Deng, X. Zheng, J. Fang, Y. Yang, Progressive nitrogen limitation across the Tibetan alpine permafrost region. *Nat. Commun.* **11**, 3331 (2020).

19. W. Taihua, Y. Dawen, Y. Yuting, P. Shilong, L. Xin, C. Guodong, F. Bojie, Permafrost thawing puts the frozen carbon at risk over the Tibetan Plateau. *Sci. Adv.* **6**, eaaz3513 (2020).

20. J. Ding, L. Chen, C. Ji, G. Hugelius, Y. Li, L. Liu, S. Qin, B. Zhang, G. Yang, F. Li, K. Fang, Y. Chen, Y. Peng, X. Zhao, H. He, P. Smith, J. Fang, Y. Yang, Decadal soil carbon accumulation across Tibetan permafrost regions. *Nat. Geosci.* **10**, 420–424 (2017).

21. S. Piao, K. Tan, H. Nan, P. Ciais, J. Fang, T. Wang, N. Vuichard, B. Zhu, Impacts of climate and CO_2 changes on the vegetation growth and carbon balance of Qinghai–Tibetan grasslands over the past five decades. *Glob. Planet. Change* **98-99**, 73–80 (2012).

22. Q. Zhuang, J. He, Y. Lu, L. Ji, X. Xiao, T. Luo, Carbon dynamics of terrestrial ecosystems on the Tibetan Plateau during the 20th century: An analysis with a process-based biogeochemical model. *Glob. Ecol. Biogeogr.* **19**, 649–662 (2010).

23. K. Tan, P. Ciais, S. Piao, X. Wu, Y. Tang, N. Vuichard, S. Liang, J. Fang, Application of the ORCHIDEE global vegetation model to evaluate biomass and soil carbon stocks of Qinghai-Tibetan grasslands. *Glob. Biogeochem. Cycle* **24**, GB1013 (2010).

24. Y. Ma, Z. Hu, Z. Xie, W. Ma, B. Wang, X. Chen, M. Li, L. Zhong, F. Sun, L. Gu, C. Han, L. Zhang, X. Liu, Z. Ding, G. Sun, S. Wang, Y. Wang, Z. Wang, A long-term (2005–2016) dataset of hourly integrated land–atmosphere interaction observations on the Tibetan Plateau. *Earth Syst. Sci. Data* **12**, 2937–2957 (2020).

25. Y. Wang, J. Xiao, Y. Ma, Y. Luo, Z. Hu, F. Li, Y. Li, L. Gu, Z. Li, L. Yuan, Carbon fluxes and environmental controls across different alpine grassland types on the Tibetan Plateau. *Agric. For. Meteorol.* **311**, 108694 (2021).

26. D. Wei, Y. Qi, Y. Ma, X. Wang, W. Ma, T. Gao, L. Huang, H. Zhao, J. Zhang, X. Wang, Plant uptake of CO_2 outpaces losses from permafrost and plant respiration on the Tibetan Plateau. *Proc. Natl. Acad. Sci. U.S.A.* **118**, e2015283118 (2021).

27. S. Sun, T. Che, H. Li, T. Wang, C. Ma, B. Liu, Y. Wu, Z. Song, Water and carbon dioxide exchange of an alpine meadow ecosystem in the northeastern Tibetan Plateau is energy-limited. *Agric. For. Meteorol.* **275**, 283–295 (2019).

28. J. A. Biederman, R. L. Scott, T. W. Bell, D. R. Bowling, S. Dore, J. Garatuza-Payan, T. E. Kolb, P. Krishnan, D. J. Krofcheck, M. E. Litvak, G. E. Maurer, T. P. Meyers, W. C. Oechel, S. A. Papuga, G. E. Ponce-Campos, J. C. Rodriguez, W. K. Smith, R. Vargas, C. J. Watts, E. A. Yepez, M. L. Goulden, CO_2 exchange and evapotranspiration across dryland ecosystems of southwestern North America. *Glob. Chang. Biol.* **23**, 4204–4221 (2017).

29. W. Liang, W. Zhang, Z. Jin, J. Yan, Y. Lü, S. Wang, B. Fu, S. Li, Q. Ji, F. Gou, S. Fu, S. An, F. Wang, Estimation of global grassland net ecosystem carbon exchange using a model tree ensemble approach. *J. Geophys. Res. Biogeosci* **125**, e2019JG005034 (2020).

30. Y. Chen, J. Feng, X. Yuan, B. Zhu, Effects of warming on carbon and nitrogen cycling in alpine grassland ecosystems on the Tibetan Plateau: A meta-analysis. *Geoderma* **370**, 114363 (2020).

31. M. Shen, S. Wang, N. Jiang, J. Sun, R. Cao, X. Ling, B. Fang, L. Zhang, L. Zhang, X. Xu, W. Lv, B. Li, Q. Sun, F. Meng, Y. Jiang, T. Dorji, Y. Fu, A. Iler, Y. Vitasse, H. Steltzer, Z. Ji, W. Zhao, S. Piao, B. Fu, Plant phenology changes and drivers on the Qinghai–Tibetan Plateau. *Nat. Rev. Earth Environ.* **3**, 633–651 (2022).

32. M. Ma, W. Yuan, J. Dong, F. Zhang, W. Cai, H. Li, Large-scale estimates of gross primary production on the Qinghai-Tibet plateau based on remote sensing data. *Int. J. Digit. Earth* **11**, 1166–1183 (2017).

33. J. Zhou, K. Xue, J. Xie, Y. Deng, L. Wu, X. Cheng, S. Fei, S. Deng, Z. He, J. D. Van Nostrand, Y. Luo, Microbial mediation of carbon-cycle feedbacks to climate warming. *Nat. Clim. Chang.* **2**, 106–110 (2011).

34. X. Zhu, C. Luo, S. Wang, Z. Zhang, S. Cui, X. Bao, L. Jiang, Y. Li, X. Li, Q. Wang, Y. Zhou, Effects of warming, grazing/cutting and nitrogen fertilization on greenhouse gas fluxes during growing seasons in an alpine meadow on the Tibetan Plateau. *Agric. For. Meteorol.* **214-215**, 506–514 (2015).

35. Q. Li, Y. Liu, D. Kou, Y. Peng, Y. Yang, Substantial non-growing season carbon dioxide loss across Tibetan alpine permafrost region. *Glob. Chang. Biol.* **28**, 5200–5210 (2022).

36. M. Saito, T. Kato, Y. Tang, Temperature controls ecosystem CO_2 exchange of an alpine meadow on the northeastern Tibetan Plateau. *Glob. Chang. Biol.* **15**, 221–228 (2009).

37. Y. Wang, Z. Zhu, Y. Ma, L. Yuan, Carbon and water fluxes in an alpine steppe ecosystem in the Nam Co area of the Tibetan Plateau during two years with contrasting amounts of precipitation. *Int. J. Biometeorol.* **64**, 1183–1196 (2020).

38. T. Zhang, Y. Zhang, M. Xu, J. Zhu, N. Chen, Y. Jiang, K. Huang, J. Zu, Y. Liu, G. Yu, Water availability is more important than temperature in driving the carbon fluxes of an alpine meadow on the Tibetan Plateau. *Agric. For. Meteorol.* **256-257**, 22–31 (2018).

39. X. Chen, G. Wang, T. Zhang, T. Mao, D. Wei, Z. Hu, C. Song, Effects of warming and nitrogen fertilization on GHG flux in the permafrost region of an alpine meadow. *Atmos. Environ.* **157**, 111–124 (2017).

40. Z. Zhao, S. Dong, X. Jiang, S. Liu, H. Ji, Y. Li, Y. Han, W. Sha, Effects of warming and nitrogen deposition on CH_4, CO_2 and N_2O emissions in alpine grassland ecosystems of the Qinghai-Tibet Plateau. *Sci. Total Environ.* **592**, 565–572 (2017).

41. Y. Zhang, Ecosystem productivity data of Qinghai Tibet Plateau under CO_2 enrichment scenario during 2018-2019 (A Big Earth Data Platform for Three Poles, 2022).

42. X. Li, Y. He, Z. Zeng, X. Lian, X. Wang, M. Du, G. Jia, Y. Li, Y. Ma, Y. Tang, W. Wang, Z. Wu, J. Yan, Y. Yao, P. Ciais, X. Zhang, Y. Zhang, Y. Zhang, G. Zhou, S. Piao, Spatiotemporal pattern of terrestrial evapotranspiration in China during the past thirty years. *Agric. For. Meteorol.* **259**, 131–140 (2018).

43. J. Zeng, T. Matsunaga, Z. H. Tan, N. Saigusa, T. Shirai, Y. Tang, S. Peng, Y. Fukuda, Global terrestrial carbon fluxes of 1999-2019 estimated by upscaling eddy covariance data with a random forest. *Sci. Data* **7**, 313 (2020).

44. D. N. Huntzinger, C. Schwalm, A. M. Michalak, K. Schaefer, A. W. King, Y. Wei, A. Jacobson, S. Liu, R. B. Cook, W. M. Post, G. Berthier, D. Hayes, M. Huang, A. Ito, H. Lei, C. Lu, J. Mao, C. H. Peng, S. Peng, B. Poulter, D. Riccuito, X. Shi, H. Tian, W. Wang, N. Zeng, F. Zhao, Q. Zhu, The North American Carbon Program Multi-Scale Synthesis and Terrestrial Model Inter-comparison Project—Part 1: Overview and experimental design. *Geosci. Model Dev.* **6**, 2121–2133 (2013).

45. Y. Wang, Z. Ding, Y. Ma, Data processing uncertainties may lead to an overestimation of the land carbon sink of the Tibetan Plateau. *Proc. Natl. Acad. Sci. U.S.A.* **119**, e2202343119 (2022).

46. B. Fang, H. Lei, Y. Zhang, Q. Quan, D. Yang, Spatio-temporal patterns of evapotranspiration based on upscaling eddy covariance measurements in the dryland of the North China Plain. *Agric. For. Meteorol.* **281**, 107844 (2020).

47. Y. Yao, X. Wang, Y. Li, T. Wang, M. Shen, M. Du, H. He, Y. Li, W. Luo, M. Ma, Y. Ma, Y. Tang, H. Wang, X. Zhang, Y. Zhang, L. Zhao, G. Zhou, S. Piao, Spatiotemporal pattern of gross primary productivity and its covariation with climate in China over the last thirty years. *Glob. Chang. Biol.* **24**, 184–196 (2018).

48. H. Wang, X. Li, J. Xiao, M. Ma, J. Tan, X. Wang, L. Geng, Carbon fluxes across alpine, oasis, and desert ecosystems in northwestern China: The importance of water availability. *Sci. Total Environ.* **697**, 133978 (2019).

49. B. Martens, D. G. Miralles, H. Lievens, R. van der Schalie, R. A. M. de Jeu, D. Fernández-Prieto, H. E. Beck, W. A. Dorigo, N. E. C. Verhoest, GLEAM v3: Satellite-based land evaporation and root-zone soil moisture. *Geosci. Model Dev.* **10**, 1903–1925 (2017).

50. X. Meng, K. Mao, F. Meng, J. Shi, J. Zeng, X. Shen, Y. Cui, L. Jiang, Z. Guo, A fine-resolution soil moisture dataset for China in 2002–2018. *Earth Syst. Sci. Data* **13**, 3239–3261 (2021).

51. S. Piao, J. Fang, P. Ciais, P. Peylin, Y. Huang, S. Sitch, T. Wang, The carbon balance of terrestrial ecosystems in China. *Nature* **458**, 1009–1013 (2009).

52. T. Yao, L. Thompson, D. Chen, S. Piao, Reflections and future strategies for third pole environment. *Nat. Rev. Earth. Environ.* **3**, 608–610 (2022).

53. L. Ma, H. C. Zuo, Quantifying net carbon fixation by Tibetan alpine ecosystems should consider multiple anthropogenic activities. *Proc. Natl. Acad. Sci. U.S.A.* **119**, e2115676119 (2022).

54. C. Song, G. Wang, Land carbon sink of the Tibetan Plateau may be overestimated without accounting for the aquatic carbon export. *Proc. Natl. Acad. Sci. U.S.A.* **118**, (2021).

55. B. Wang, H. Jin, Q. Li, D. Chen, L. Zhao, Y. Tang, T. Kato, S. Gu, Diurnal and seasonal variations in the net ecosystem CO_2 exchange of a pasture in the three-river source region of the Qinghai-tibetan plateau. *PLOS ONE* **12**, e0170963 (2017).

56. X. Liu, D. Zhu, W. Zhan, H. Chen, Q. Zhu, Y. Hao, W. Liu, Y. He, Five-year measurements of net ecosystem CO_2 exchange at a fen in the Zoige peatlands on the Qinghai-Tibetan Plateau. *J. Geophys. Res. Atmos.* **124**, 11803–11818 (2019).

57. Y. Qi, D. Wei, H. Zhao, X. Wang, Carbon sink of a very high marshland on the Tibetan Plateau. *J. Geophys. Res. Biogeo.* **126**, e2020JG006235 (2021).

58. T. Wutzler, A. Lucas-Moffat, M. Migliavacca, J. Knauer, K. Sickel, L. Šigut, O. Menzer, M. Reichstein, Basic and extensible post-processing of eddy covariance flux data with REddyProc. *Biogeosciences* **15**, 5015–5030 (2018).

59. Y. Yao, P. Ciais, N. Viovy, W. Li, F. Cresto-Aleina, H. Yang, E. Joetzjer, B. Bond-Lamberty, A data-driven global soil heterotrophic respiration dataset and the drivers of its inter-annual variability. *Glob. Biogeochem. Cycle* **35**, e2020GB006918 (2021).

60. X. Li, J. Xiao, Mapping photosynthesis solely from solar-induced chlorophyll fluorescence: A global, fine-resolution dataset of gross primary production derived from OCO-2. *Remote Sens.* **11**, 2563 (2019).

61. J. He, K. Yang, W. Tang, H. Lu, J. Qin, Y. Chen, X. Li, The first high-resolution meteorological forcing dataset for land process studies over China. *Sci. Data* **7**, 25 (2020).

62. L. Breiman, Random forests. *Mach. Learn.* **45**, 5–32 (2001).

63. P. Geurts, D. Ernst, L. Wehenkel, Extremely randomized trees. *Mach. Learn.* **63**, 3–42 (2006).

64. T. Chen, T. He, M. Benesty, Xgboost: Extreme gradient boosting. *R package version 0.4-2*, 1–4 (2015).

65. S. Sun, H. Chen, G. Sun, W. Ju, G. Wang, X. Li, G. Yan, C. Gao, J. Huang, F. Zhang, S. Zhu, W. Hua, Attributing the changes in reference evapotranspiration in southwestern china using a new separation method. *J. Hydrometeorol.* **18**, 777–798 (2017).

66. Z. Zhao, H. Wang, C. Wang, W. Li, H. Chen, C. Deng, Changes in reference evapotranspiration over Northwest China from 1957 to 2018: Variation characteristics, cause analysis and relationships with atmospheric circulation. *Agric. Water Manag.* **231**, 105958 (2020).

67. S. Li, G. Wang, S. Sun, D. Fiifi Tawia Hagan, T. Chen, H. Dolman, Y. Liu, Long-term changes in evapotranspiration over China and attribution to climatic drivers during 1980–2010. *J. Hydrol.* **595**, 126037 (2021).

68. W. Jiao, L. Wang, W. K. Smith, Q. Chang, H. Wang, P. D'Odorico, Observed increasing water constraint on vegetation growth over the last three decades. *Nat. Commun.* **12**, 3777 (2021).